

# Assessing the Atmospheric Response to Subgrid Surface Heterogeneity in CESM2

Megan Fowler<sup>1</sup>, Richard B Neale<sup>1</sup>, Jason S Simon<sup>2</sup>, David M Lawrence<sup>1</sup>, Nathaniel W Chaney<sup>2</sup>, Paul A Dirmeyer<sup>3</sup>, Vincent E Larson<sup>4</sup>, Meng Huang<sup>5</sup>, and John Truesdale<sup>1</sup>

<sup>1</sup>National Center for Atmospheric Research

<sup>2</sup>Duke University

<sup>3</sup>George Mason University

<sup>4</sup>University of Wisconsin-Milwaukee

<sup>5</sup>Pacific Northwest National Laboratory

December 7, 2022

## Abstract

Land-atmosphere interactions are central to the evolution of the atmospheric boundary layer and the subsequent formation of clouds and precipitation. Existing global climate models represent these connections with bulk approximations on coarse spatial scales, but observations suggest that small-scale variations in surface characteristics and co-located turbulent and momentum fluxes can significantly impact the atmosphere. Recent model development efforts have attempted to capture this phenomenon by coupling existing representations of subgrid-scale (SGS) heterogeneity between land and atmosphere models. Such approaches are in their infancy and it is not yet clear if they can produce a realistic atmospheric response to surface heterogeneity. Here, we implement a parameterization to capture the effects of SGS heterogeneity in the Community Earth System Model (CESM2), and compare single-column simulations against high-resolution Weather Research and Forecasting (WRF) large-eddy simulations (LESs), which we use as a proxy for observations. The CESM2 experiments increase the temperature and humidity variances in the lowest atmospheric levels, but the response is weaker than in WRF-LES. In part, this is attributed to an underestimate of surface heterogeneity in the land model due to a lack of SGS meteorology, a separation between deep and shallow convection schemes in the atmosphere, and a lack of explicitly represented mesoscale secondary circulations. These results highlight the complex processes involved in capturing the effects of SGS heterogeneity and suggest the need for parameterizations that communicate their influence not only at the surface but also vertically.

1     **Assessing the Atmospheric Response to Subgrid Surface Heterogeneity in CESM2**

2     **Megan D. Fowler<sup>1</sup>, Richard B. Neale<sup>1</sup>, Jason S. Simon<sup>2,3</sup>, David M. Lawrence<sup>1</sup>, Nathaniel**  
3     **W. Chaney<sup>2</sup>, Paul A. Dirmeyer<sup>4</sup>, Vincent E. Larson<sup>5,6</sup>, Meng Huang<sup>6</sup>, and John Truesdale<sup>1</sup>**

4     <sup>1</sup> National Center for Atmospheric Research, Boulder, CO, USA

5     <sup>2</sup> Duke University, Durham, NC, USA

6     <sup>3</sup> Saint Augustine's University, Raleigh, NC, USA

7     <sup>4</sup> George Mason University, Fairfax, VA, USA

8     <sup>5</sup> University of Wisconsin-Milwaukee, Milwaukee, WI, USA

9     <sup>6</sup> Pacific Northwest National Laboratory, Richland, WA, USA

10    Corresponding author: Megan D. Fowler ([mdfowler@ucar.edu](mailto:mdfowler@ucar.edu))

11

12    **Key Points:**

- 13       • A new method of conveying information on subgrid-scale surface heterogeneity to the  
14       atmosphere is introduced to CESM2.
- 15       • A comparison with large-eddy simulations suggests that the atmospheric response to  
16       heterogeneity in CESM2 is too vertically constrained.
- 17       • Future model development efforts should focus on representing heterogeneity in ways  
18       that can explicitly capture secondary circulations.

19

## 20 **Abstract**

21 Land-atmosphere interactions are central to the evolution of the atmospheric boundary layer and  
22 the subsequent formation of clouds and precipitation. Existing global climate models represent  
23 these connections with bulk approximations on coarse spatial scales, but observations suggest  
24 that small-scale variations in surface characteristics and co-located turbulent and momentum  
25 fluxes can significantly impact the atmosphere. Recent model development efforts have  
26 attempted to capture this phenomenon by coupling existing representations of subgrid-scale  
27 (SGS) heterogeneity between land and atmosphere models. Such approaches are in their infancy  
28 and it is not yet clear if they can produce a realistic atmospheric response to surface  
29 heterogeneity. Here, we implement a parameterization to capture the effects of SGS  
30 heterogeneity in the Community Earth System Model (CESM2), and compare single-column  
31 simulations against high-resolution Weather Research and Forecasting (WRF) large-eddy  
32 simulations (LESs), which we use as a proxy for observations. The CESM2 experiments increase  
33 the temperature and humidity variances in the lowest atmospheric levels, but the response is  
34 weaker than in WRF-LES. In part, this is attributed to an underestimate of surface heterogeneity  
35 in the land model due to a lack of SGS meteorology, a separation between deep and shallow  
36 convection schemes in the atmosphere, and a lack of explicitly represented mesoscale secondary  
37 circulations. These results highlight the complex processes involved in capturing the effects of  
38 SGS heterogeneity and suggest the need for parameterizations that communicate their influence  
39 not only at the surface but also vertically.

## 40 **Plain Language Summary**

41 Land surface temperature and soil moisture are known to influence the daily evolution of the  
42 overlying atmosphere and the formation of clouds and rainfall. While global climate models  
43 represent these interactions on relatively coarse spatial scales (i.e., 100 km or greater), smaller  
44 scale differences in surface characteristics are increasingly recognized for their ability to impact  
45 the atmosphere. Here, we implement a new feature in a climate model that communicates  
46 information on small-scale surface differences from the land to the atmospheric model. We  
47 compare the results of this addition against a high-resolution model that has previously been used  
48 to isolate the impacts of surface flux gradients, with the latter serving as a proxy for  
49 observations. Though there are some encouraging signs of the implemented approach to drive an  
50 atmospheric response to surface variability, we find that a missing representation of large-scale  
51 circulations between warm/cool surfaces likely limits model agreement.

## 52 **1 Introduction**

53 The land surface has a well-documented ability to influence planetary boundary layer (PBL)  
54 characteristics (Avisar & Pielke, 1989; Brunsell et al., 2011; H. Huang & Margulis, 2013;  
55 Hubbe et al., 1997; Kustas & Albertson, 2003; Mahrt, 2000), clouds and precipitation (Berg &  
56 Stull, 2005; Kang, 2016; Pielke Sr., 2001; Rieck et al., 2014; Schrieber et al., 1996), and  
57 hydrometeorological extremes (Fischer et al., 2007; Hirschi et al., 2011; Mocko et al., 2021;  
58 Santanello et al., 2015; Dirmeyer et al., 2021). Even relatively small scale surface features create  
59 important temperature and moisture gradients, such as between rivers/lakes and adjacent land  
60 (Ramos da Silva et al., 2011; Y. Zhang et al., 2021), or between urban and rural regions  
61 (Hjelmfelt, 1982; Baik et al., 2001; Dixon and Mote, 2003; Shepherd, 2005; Shem and Shepherd,  
62 2009); those contrasts are often enough to drive a convective response. The horizontal scale at

63 which land-atmosphere interactions occur can thus be finer than what is resolved by relatively  
64 coarse global climate models (GCMs) with resolutions  $\geq 100$  km. A critical challenge for Earth  
65 system modeling has been how to represent the atmospheric impacts of such small-scale surface  
66 heterogeneity (Bou-Zeid et al., 2020; Schrieber et al., 1996).

67 A common strategy for representing subgrid-scale (SGS) surface heterogeneity ( $\mathcal{O}(1)$ - $\mathcal{O}(10)$  km)  
68 within land models has been to use a tiling approach, where each gridcell contains a statistical  
69 representation of the land cover types within it (e.g., urban, forested, etc.). Each tile is then  
70 characterized by unique surface fluxes/states that contribute to the grid-mean average based on  
71 the percent of gridcell area it covers. Avissar and Pielke (1989) proposed this approach after  
72 noting the role that differences in sensible heat flux played on PBL development, and subsequent  
73 studies have found substantial improvements when using this approach (Koster & Suarez, 1992;  
74 Hahmann & Dickinson, 2001; Dai et al., 2003; Li et al., 2013). This is especially critical at the  
75 current spatial scales of GCMs (i.e., 50-100 km), where variations in land cover are almost  
76 guaranteed within a single gridcell.

77 A tiling scheme as described above represents SGS surface heterogeneity within a land model,  
78 but it continues to pass only grid-mean surface fluxes to the atmosphere. From an atmospheric  
79 perspective then, any information on SGS heterogeneity in surface forcing is lost. Several  
80 studies, however, highlight the importance of this information in the development of clouds and  
81 rainfall. Berg and Stull (2005) suggest that the formation of boundary layer cumulus clouds can  
82 be tied directly to a joint probability density function (PDF) of virtual potential temperature and  
83 water vapor mixing ratio over a heterogeneous surface. Others have highlighted the ability of  
84 horizontal gradients in surface fluxes, temperature, and soil moisture to generate secondary  
85 circulations that redistribute energy and moisture (Ookouchi et al., 1984; Doran et al., 1995;  
86 Avissar & Schmidt, 1998; Bou-Zeid et al., 2020; Cheng et al., 2021). Those circulations play a  
87 key role in cloud and rainfall development (Cheng et al., 2021; Graf et al., 2021; Taylor et al.,  
88 2011; Avissar & Liu, 1996).

89 A recent LES study was designed to directly assess the importance of representing SGS  
90 heterogeneity by specifying surface boundary conditions that either allow for varying surface  
91 fluxes or are constant across the domain (Simon et al., 2021). Allowing surface fluxes to vary  
92 spatially was found to increase domain-average turbulence and cloud liquid water path by  
93 helping to organize convection and precipitation. Gradients in surface fluxes within a single 100  
94 km domain can therefore generate mesoscale secondary circulations capable of altering the grid-  
95 mean environment (Simon et al., 2021).

96 Recent GCM-based studies have attempted to move beyond a reliance on gridcell means by  
97 exploring mechanisms that link existing parameterizations of SGS variability. M. Huang et al.  
98 (2022), hereafter H22, introduced such a scheme into the Energy Exascale Earth System Model  
99 version 1 (E3SMv1). The approach utilizes the turbulence and boundary layer scheme, Cloud  
100 Layers Unified By Binormals (CLUBB; Golaz et al., 2002; Larson et al., 2002), which estimates  
101 near-surface temperature and humidity variances and their covariance from grid-mean fluxes. To  
102 capture SGS surface heterogeneity, H22 added a term to CLUBB's boundary conditions to  
103 represent the differences in temperature and moisture present across SGS surface tiles. Single-  
104 column experiments at the Department of Energy's Atmospheric Radiation Measurement (ARM)  
105 Southern Great Plains (SGP) site during the summer of 2015 suggested that the addition drives a

106 slight increase in liquid water path on non-precipitating days. This is qualitatively in agreement  
 107 with the results of Simon et al. (2021), but it remains to be seen how such a parameterization  
 108 verifies against similar LES experiments. Although LESs are not perfect proxies for  
 109 observations, the model framework established by Simon et al. (2021) allows a direct  
 110 comparison between identical atmospheric conditions when treating the surface as homogeneous  
 111 vs. heterogeneous. We thus consider it a reasonable approximation for how the atmosphere  
 112 responds to SGS heterogeneity.

113 In this study, we implement a similar approach to what was used in H22 to convey information  
 114 on SGS surface heterogeneity to the atmosphere within the Community Earth System Model  
 115 (CESM2). The two models have similar physics in both the atmosphere and land model  
 116 components, though here we also enable interactive coupling between the land and atmosphere  
 117 during model run-time. More importantly, rather than investigating the ability of this  
 118 parameterization to impact the atmosphere as in H22, we focus instead on the parameterization's  
 119 ability to drive a similar atmospheric response to SGS heterogeneity as is present in a matching  
 120 set of Weather Research and Forecasting (WRF) LES simulations. A set of single-column  
 121 experiments are conducted at the SGP site to conduct this evaluation, with details on the  
 122 methodology and experiment setup provided in Section 2. In Section 3, we explore the response  
 123 to heterogeneity in these experiments and evaluate the signal relative to WRF-LES. We conclude  
 124 in Section 4 with a summary of the main results from this analysis and their broader  
 125 implications.

126

## 127 **2 Methods**

### 128 **2.1 Representing surface heterogeneity in CESM2**

129 As in E3SMv1, the CESM2 atmosphere and land models contain separate representations of SGS  
 130 heterogeneity. In the Community Atmosphere Model (CAM6), this is again through CLUBB,  
 131 which assumes a joint PDF to predict means and higher-order moments of liquid water potential  
 132 temperature ( $\theta_l$ ), total water specific humidity ( $q_t$ ), and vertical velocity ( $w$ ). The parameters of  
 133 this joint PDF depend on the grid-mean values of those fields ( $\bar{\theta}_l, \bar{q}_t, \bar{w}$ ), their SGS variances  
 134 ( $\overline{\theta_l'^2}, \overline{q_t'^2}, \overline{w'^2}$ ) and covariances ( $\overline{\theta_l'q_t'}, \overline{w'q_t'}, \overline{w'\theta_l'}$ ), and higher-order moments. The latter  
 135 includes the skewness of vertical velocity ( $\overline{w'^3}$ ) to represent the asymmetry of turbulent  
 136 updrafts/downdrafts in CLUBB, which is explicitly represented in WRF-LES. In this notation,  
 137 overbars denote grid-mean values and primes indicate SGS values (i.e., departures from the grid  
 138 mean). Third and fourth order moments are found from individual closure assumptions.

139

140 Importantly, not all higher-order moments are computed at each vertical level. CLUBB is  
 141 implemented on a staggered grid such that the level interfaces (vs. midpoints) only compute the  
 142 second-order moments. At the lowest model level interface, assumed to be in contact with the  
 143 surface, the primary focus is on the (co)variances of temperature and humidity since  $\bar{w}$  is  
 144 assumed to be zero. We follow the original formulation laid out in André et al. (1978) to  
 145 compute these in CLUBB (i.e., the flag `l_andre_1978` is set to true within CLUBB):

146

$$147 \quad \overline{\theta_l'^2}_{HOM} = \frac{Q_o^2}{u_*^2} \left[ 4(1 - 8.3\zeta)^{\frac{2}{3}} \right] \quad \zeta < 0 \quad (1)$$

$$148 \quad = \frac{Q_o^2}{u_*^2} [4] \quad \zeta > 0$$

$$149$$

$$150 \quad \overline{q_t'^2}_{HOM} = \frac{H_o^2}{u_*^2} \left[ 4(1 - 8.3\zeta)^{\frac{2}{3}} \right] \quad \zeta < 0 \quad (2)$$

$$151 \quad = \frac{H_o^2}{u_*^2} [4] \quad \zeta > 0$$

$$152$$

$$153 \quad \overline{\theta_l' q_t'}_{HOM} = \sqrt{\overline{\theta_l'^2}} \sqrt{\overline{q_t'^2}} \quad (3)$$

154  
 155 Where  $u_*$  is the friction velocity,  $\zeta$  is the Monin-Obukhov stability parameter,  $Q_o$  ( $H_o$ ) is the  
 156 kinematic heat (moisture) flux. The subscript *HOM* indicates that these moments are computed  
 157 assuming a homogeneous surface; that is, they depend only on grid-mean fluxes that are passed  
 158 to CAM6 from the surface model. These second order moments are currently computed within  
 159 CLUBB, but computing them in the surface model instead would make additional information on  
 160 tile-level characteristics readily available.

161  
 162 The Community Land Model (CLM5; Lawrence et al., 2019) represents SGS land heterogeneity  
 163 with a tiling approach, statistically dividing the area of each gridcell between different surface  
 164 types. The version of CLM5 used here prescribes vegetation phenology and has no active  
 165 biogeochemical component, resulting in 17 surface types that include urban areas, lakes, glaciers,  
 166 bare soil, various plant functional types, and irrigated and rain-fed crops. Each surface tile is  
 167 characterized by unique near-surface temperature, humidity, surface fluxes, friction velocity, and  
 168 stability parameter values. These calculations use grid-mean quantities from the lowest model  
 169 level of the atmosphere, either directly (e.g., temperature) or indirectly (e.g., 10-m wind speed).  
 170 There is therefore no accounting for SGS meteorology at the land surface.

171  
 172 Building on theory proposed in Machulskaya and Mironov (2018), H22 added a new connection  
 173 between near-surface CLUBB (co)variances and surface tiling schemes. The essence of the  
 174 approach stems from the assumption that any grid-mean variable can be represented as the sum  
 175 of two parts: the mean value and the SGS fluctuations around that mean. This is applied to the  
 176 higher-order moments above as follows:

$$177$$

$$178 \quad \overline{\theta_l'^2}_{HET} = \overline{\theta_l'^2}_{HOM} + \overline{(\theta_{l,tile} - \bar{\theta}_l)^2} \quad (4)$$

$$179$$

$$180 \quad \overline{q_t'^2}_{HET} = \overline{q_t'^2}_{HOM} + \overline{(q_{t,tile} - \bar{q}_t)^2} \quad (5)$$

$$181$$

$$182$$

$$183 \quad \overline{\theta_l' q_t'}_{HET} = \overline{\theta_l' q_t'}_{HOM} + \overline{(\theta_{l,tile} - \bar{\theta}_l)(q_{t,tile} - \bar{q}_t)} \quad (6)$$

184

185 The heterogeneous representation of these moments is thus the sum of the homogeneous  
 186 calculation and the departure of each tile’s temperature and humidity from the grid-mean value.  
 187 The most efficient way to incorporate the heterogeneous term is to move the calculation of  
 188 CLUBB’s boundary conditions into CLM5. Thus the values of  $\overline{\theta_l'^2}$ ,  $\overline{q_t'^2}$ , and  $\overline{\theta_l'q_t'}$ , along with  
 189  $\overline{w'^2}$ ,  $\overline{u'^2}$  and  $\overline{v'^2}$  are computed from tile-level data in the land model (with or without an  
 190 additional heterogeneous term) and averaged to the gridcell level before being passed to CAM6  
 191 for use in CLUBB.

192

## 193 2.2 Modeling Experiments

194 We examine the impact of this parameterization in single-column atmospheric model  
 195 experiments (SCAM6; Gettelman et al., 2019) at the ARM SGP site, with the distribution of  
 196 surface tiles described in Table 1. A set of control experiments follow the homogeneous  
 197 approach of computing surface moments (*HOM*) and are compared with a set of experiments that  
 198 use the new heterogeneous approach (*HET*). In all SCAM experiments, we increase the  
 199 atmospheric vertical resolution from 32 to 64 levels in order to better resolve PBL processes. The  
 200 coupling frequency between the land and atmosphere is also decreased from 20 to 5 minutes. The  
 201 simulations prescribe the horizontal winds and temperature/moisture advection from the LASSO  
 202 VARANAL dataset (Gustafson et al., 2019), a coarsened version of the same large-scale forcing  
 203 that was used in Simon et al. (2021). Though not quite identical to the WRF-LES boundary  
 204 forcing as a result of fewer vertical levels, the two are indeed similar. There is thus little reason  
 205 to suspect that this is a primary driver of potential model disagreement, given the other pathways  
 206 by which SCAM and WRF-LES diverge (i.e., convection and microphysical schemes, land  
 207 surface models, etc.). Surface fields (i.e., surface fluxes, near-surface temperature and humidity,  
 208 etc.) are allowed to evolve freely. SCAM is run at a T42 ( $\sim 2.8^\circ$ ) resolution, with SGS surface tile  
 209 distributions defined at the same resolution.

210

211 **Table 1:** Distribution of surface tiles in CLM5 at the gridcell containing the SGP site.

Surface Type	Percent of Total Grid Area (%)
C3 crop	48.74
C3 grass	25.56
C4 grass	22.17
C3 irrigated crop	2.26
Broadleaf deciduous temperate tree	0.66
Bare ground	0.32
Needleleaf evergreen temperate tree	0.15
Urban	0.15

212

213 As in H22, SCAM simulations follow a hindcast approach: the model is run for two days,  
 214 discarding the first day for model spin-up and using the second day for analysis. Unlike in H22  
 215 however, we do not create a continuous time series of summer (June-August) days in 2015.  
 216 Instead, we select days that have been simulated by WRF-LES as part of an extension to Simon  
 217 et al. (2021), which are documented in Simon et al. (2022).

218

219 Simon et al. (2021) simulated three shallow convection days at the ARM SGP site using WRF-  
 220 LES (Skamarock et al., 2008). On each day, a 100x100 km domain was forced by either  
 221 homogeneous or heterogeneous surface conditions. In the heterogeneous case, an offline land

222 model (HydroBlocks; Chaney et al., 2016) was used to supply prescribed surface fluxes,  
 223 temperature, albedo, and momentum drag coefficients to each atmospheric column. The  
 224 homogeneous case forces every column by the grid-mean values of these terms instead. Since  
 225 those initial experiments were conducted, the work has expanded to include 92 shallow  
 226 convection days (Simon et al., 2022). The increased temporal sampling necessitated a  
 227 degradation in horizontal resolution to 250x250 m (compared to 100 m in the original set of three  
 228 days), and covers a slightly larger domain of 130 x 130 km.

229  
 230 In this study, we focus on the warm season when land-atmosphere interactions in the central  
 231 United States are strongest. We therefore simulate a subset of all available WRF-LES days,  
 232 covering 60 days between May and September in 2015-2018. All LES-based analysis is limited  
 233 to this subset of 60 days as well. We search for a similar atmospheric signal in SCAM as was  
 234 seen in WRF-LES: increased turbulence relative to *HOM* and increases in  $\overline{\theta'_t{}^2}$ , and  $\overline{q'_t{}^2}$ . We are  
 235 not attempting to align the control cases between WRF-LES and SCAM in this study. There are  
 236 a number of reasons to anticipate the two may not agree regardless, including differences in the  
 237 land models providing the surface forcing and the formation of organized convection and rainfall  
 238 in LES, which is difficult to capture in SCAM. Instead, we compare the relative atmospheric  
 239 change between *HET* and *HOM* cases across models. Two sets of SCAM sensitivity experiments  
 240 are also conducted to determine the impacts of stronger surface heterogeneity and a continuous  
 241 convection scheme. These are introduced in Section 3.3, but are included in Table 2 as a  
 242 reference for all SCAM experiments conducted.

243  
 244 **Table 2:** Single-column CESM2 experiments and descriptions.

SCAM Experiment	Description
<i>HOM</i>	Following the original equations laid out in André et al. (1978) in Eq. 1-3, this is roughly analogous to the default behavior of CLUBB in CESM2.
<i>HET</i>	Surface variances of temperature and moisture are modified to include a heterogeneous term, as in Eq. 4-6.
<i>HET<sub>a</sub></i>	As in <i>HET</i> , but with the SGS surface variances in Eq. 4-6 scaled to match the lowest model level daily maximum variance in WRF-LES.
<i>HOM<sub>noDC</sub></i>	As in <i>HOM</i> , but with the default deep convection scheme turned off so that CLUBB is responsible for both shallow and deep convection.
<i>HET<sub>noDC</sub></i>	As in <i>HOM<sub>noDC</sub></i> , but with the CLUBB surface variances modified to include the effects of SGS heterogeneity as in <i>HET</i> .
<i>HET<sub>a,noDC</sub></i>	As in <i>HET<sub>noDC</sub></i> , but with the magnitude of SGS surface variances scaled to match the LES experiments as in <i>HET<sub>a</sub></i> .

245

## 246 3 Results

### 247 3.1 Atmospheric response to surface heterogeneity in SCAM

248 The diurnal evolution of several CLUBB variables in *HOM* are shown in the left column of  
 249 Figure 1. Each variable has been interpolated from the model's raw hybrid coordinates to

250 constant pressure levels from 970-200 hPa with a 10 hPa resolution. The 60-day record  
 251 simulated by SCAM is then averaged to define composite *HOM* and *HET* cases.

252

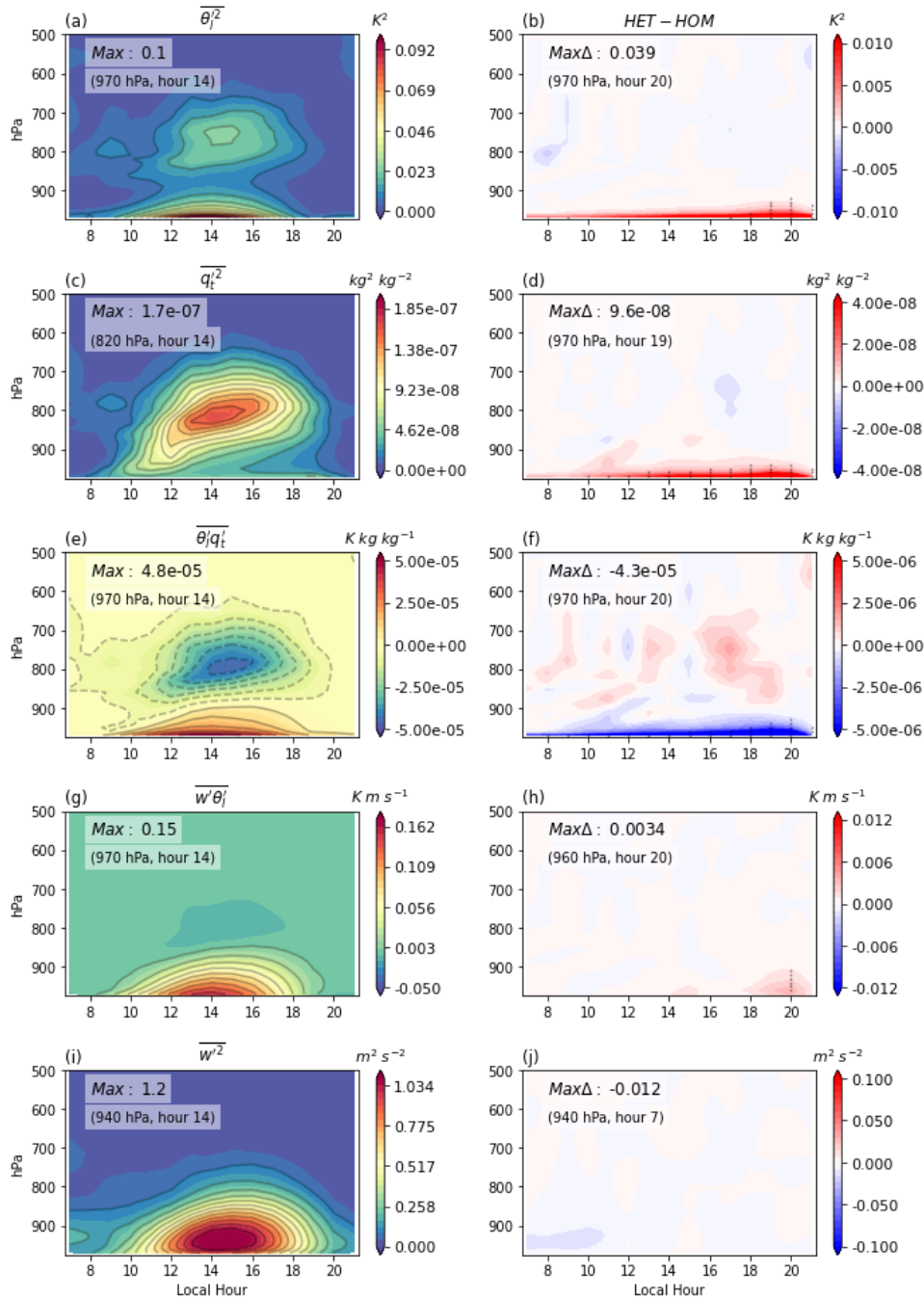
253 As the surface warms, *HOM*  $\overline{\theta_l'^2}$  peaks at 0.1 K<sup>2</sup> in the lowest model level at 14 local time (LT)  
 254 (*Fig. 1a*). Variances greater than 0.05 K<sup>2</sup> are confined to the lowest model levels, but a weaker  
 255 secondary peak occurs near the top of the PBL. The maximum of  $\overline{q_t'^2}$  occurs closer to the top of  
 256 the PBL as well, at 820 hPa (*Fig. 1c*). Both peaks along the upper boundary of the PBL are  
 257 driven by entrainment between the near-surface layer and free troposphere; near that boundary,  
 258 as warmer/drier air mixes with cooler/wetter air, the covariance between the two fields becomes  
 259 negative (*Fig. 1e*). As the co(variances) grow during the day, PBL turbulence increases as well  
 260 due to an increase in the turbulent heat flux ( $\overline{w'\theta_l'}$ ) (*Fig. 1g,i*). Note that CLUBB represents  
 261 atmospheric turbulence only through  $\overline{w'^2}$  which evolves following Eq. 7 (adapted from Larson  
 262 (2017)):

263

$$264 \quad \frac{\partial \overline{w'^2}}{\partial t} = \overline{w} \frac{\partial \overline{w'^2}}{\partial z} - \frac{1}{\rho_s} \frac{\partial \rho_s \overline{w'^3}}{\partial z} - 2 \overline{w'^2} \frac{\partial \overline{w}}{\partial z} + \frac{2g}{\theta_{vs}} \overline{w'\theta_v'} - \frac{2}{\rho_s} \overline{w' \frac{\partial p'}{\partial z}} - \epsilon_{ww} \quad (7)$$

265

266 Where  $\rho_s$  is the basic state air density,  $\theta_{vs}$  is the dry, base-state virtual potential temperature,  $g$   
 267 is the gravitational acceleration, and  $\epsilon_{ww}$  is the turbulent dissipation.



268

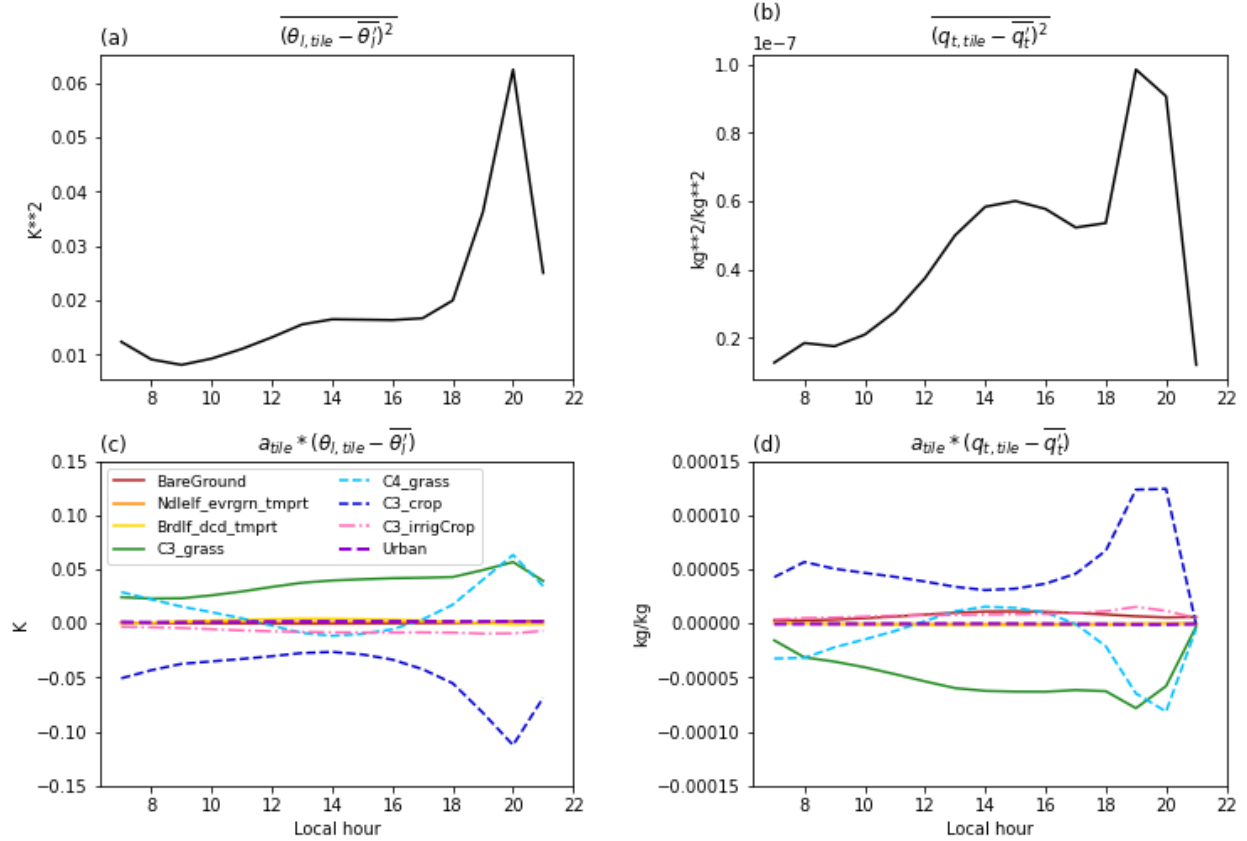
269 **Figure 1:** Time-height plots of (left) HOM temperature variance (a), moisture variance (c), their  
 270 covariance (e), eddy-flux of temperature (g), and vertical velocity variance (i), averaged over all  
 271 60 days; and (right) HET-HOM for each variable. Stippling indicates significant differences at  
 272 the 95% confidence level based on the standard error (defined as the standard deviation  
 273 normalized by the square root of the number of samples) at each hour/level. Inset text provides  
 274 the timing/height of the maximum value within the range of levels shown.  
 275

276 When SGS heterogeneity is included in the calculation of the near-surface moments,  $\overline{\theta_t'^2}$  and  $\overline{q_t'^2}$   
 277 increase relative to HOM (Fig. 1b,d). The increase, however, is statistically significant only

278 below 920 hPa (stippling in *Fig. 1* denotes significance at the 95% confidence level, determined  
 279 by the standard error). Significant increases in  $\overline{\theta'_i{}^2}$  are also limited temporally, from  $\sim$ 17-21 LT  
 280 and maximizing at 20 LT. The  $\overline{q'_t{}^2}$  increases in *HET* are statistically significant for a more  
 281 extended period of 10 LT onwards, though again the change is largest in the evening (9.6e-8  
 282 kg<sup>2</sup>/kg<sup>2</sup> at 19 LT). The covariance  $\overline{\theta'_i q'_t}$  decreases in *HET* at a magnitude that is statistically  
 283 significant for most hours as well, with a maximum change of -4.3e-5 K kg/kg (*Fig. 1f*). During  
 284 the evening hours, that decrease is enough to reverse the sign of  $\overline{\theta'_i q'_t}$  such that it becomes  
 285 negative at the lowest level (i.e., positive temperature anomalies are associated with negative  
 286 moisture anomalies) and limits the turbulent moisture flux (not shown). Ultimately then, the  
 287 addition of SGS heterogeneity does not act to increase the absolute peak of temperature/humidity  
 288 (co)variances, which occurs in the afternoon. Instead, *HET* enhances these values in the late  
 289 evening. At the timing of peak differences, *HOM*  $\overline{\theta'_i{}^2}$  has dropped to 0.01 K<sup>2</sup>,  $\overline{q'_t{}^2}$  to 4.8e-8  
 290 kg<sup>2</sup>/kg<sup>2</sup>, and  $\overline{\theta'_i q'_t}$  to 1.0e-5 K kg/kg, all well below their diurnal maximum.

291  
 292 To better understand how and why the inclusion of SGS heterogeneity increases near-surface  
 293  $\overline{\theta'_i{}^2}$  and  $\overline{q'_t{}^2}$  in the evening and reverses the sign of  $\overline{\theta'_i q'_t}$ , we evaluate the tile-level temperature  
 294 and moisture values in CLM5. Their departures from the gridcell-mean are all that differentiate  
 295 the *HET* and *HOM* calculations in Eq. 4-6. Figure 2 shows the diurnal cycle of the grid-mean  
 296 variance in temperature (*Fig. 2a*) and moisture (*Fig. 2b*), again averaged over all 60-days that  
 297 were simulated. That is, the top row of Figure 2 shows the second term in Eq. 4-6 that represents  
 298 the addition of heterogeneity. As expected, the timing of the largest variances align with the  
 299 hours where *HET* differences in Figure 1 peak and are statistically significant.

300  
 301 Note that the diurnal cycle of these patch-level variances differ from the typical diurnal cycle of  
 302 near-surface temperature and humidity, and from the timing of maximum variance in *HOM*.  
 303 Although grid-mean 2-m temperature typically peaks in the late afternoon and its variance peaks  
 304 slightly earlier than that in the control case, the SGS surface variance simulated by CLM5 does  
 305 not peak until  $\sim$ 20 LT. The evening maximum here is primarily the result of more rapid cooling  
 306 over the C3 rain-fed crop patch, covering almost half of the gridcell, compared to a slower  
 307 cooling rate over C4 and C3 grasses, which combined cover just over 47% of the grid area (dark  
 308 blue dashed line vs. dashed cyan and solid green lines respectively, *Fig. 2c*). These differential  
 309 cooling rates occur while the mean high-level cloud fraction is greater than 50% during the  
 310 evening, with a longwave cloud forcing of  $\sim$ 3.5 W/m<sup>2</sup> (thus, this is not a clear-sky signal). The  
 311 moisture variance in CLM5 also peaks in the evening but increases more steadily throughout the  
 312 day as the humidity over C3 grasses tends to remain lower than the grid mean while the moisture  
 313 over crops remains higher, with the differences between those two tiles peaking between 18-20  
 314 LT. That largely results from a higher transpiration rate in rain-fed crops compared to grasses,  
 315 which creates a more humid and cooler near-surface over C3 crops and drives a negative  
 316 covariance between temperature and moisture at the patch-level. In the evening, when the *HOM*  
 317 covariance in CLUBB has dropped to a small but still positive value, the large negative  
 318 covariance in *HET* reverses the overall signal at the lowest model level.

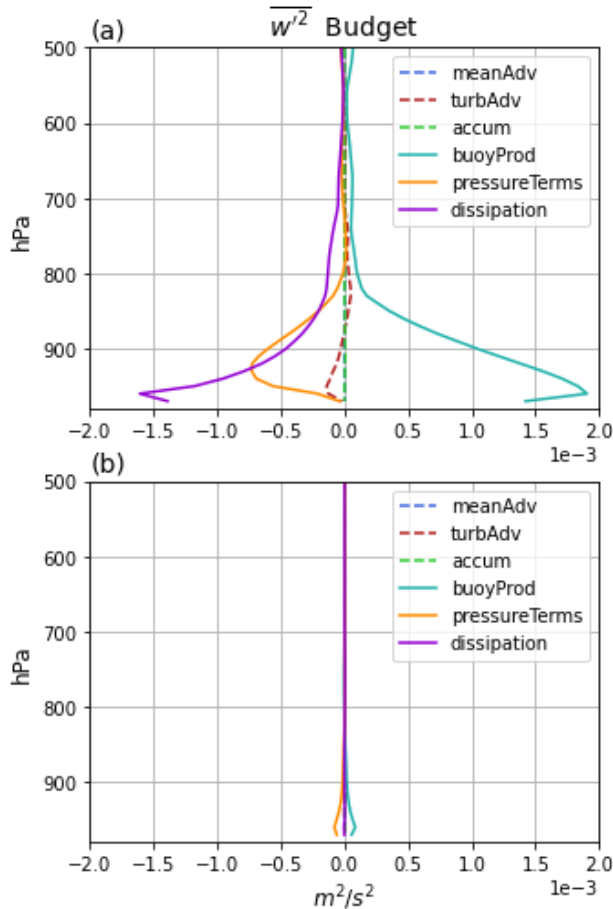


319  
 320 **Figure 2:** Mean diurnal cycles of variance across surface patch (a) temperature and (b)  
 321 humidity. (c, d) The grid area-weighted difference in temperature and humidity for each patch  
 322 relative to the gridcell mean value, which is used to compute the grid mean variances.  
 323

324 Although the near-surface higher-order moments evolve as expected in *HET*, the impacts on  
 325 atmospheric turbulence are limited. Based on the findings of Simon et al. (2021), SGS surface  
 326 heterogeneity is expected to increase PBL turbulence. Yet there are no statistically significant  
 327  $\overline{w'^2}$  increases in CLUBB (*Fig. 1j*) despite small increases in  $\overline{w'\theta_v'}$  (*Fig. 1h*). This is likely a  
 328 result of WRF-LES explicitly representing the phenomena that generate increases in turbulent  
 329 kinetic energy (TKE); CLUBB does not resolve those actual processes and instead relies on  
 330 parameterizations of their source terms. That parameterization, however, allows us to better  
 331 understand how changing the near-surface (co)variances in temperature and/or moisture could  
 332 drive an increase in turbulence.  
 333

334 Mathematically, an increase in atmospheric turbulence is achievable in CLUBB through an  
 335 increase in  $\overline{\theta_l'^2}$ . The time-evolving vertical velocity variance (Eq. 7) depends in part on a  
 336 buoyancy production term,  $\frac{2g}{\theta_{vs}} \overline{w'\theta_v'}$ , and thus the grid-mean eddy flux of virtual potential  
 337 temperature. This turbulent temperature flux is in turn dependent on the temperature variance  
 338 through its inclusion in the buoyancy production term of Eq. 3.2 in Larson (2017),  $\frac{g}{\theta_{vs}} \overline{\theta_l'\theta_v'}$ ,  
 339 where the covariance of liquid water and virtual potential temperature is tightly correlated to the  
 340 variance of liquid water potential temperature alone. Computing each term of the  $\overline{w'^2}$  budget

341 following Eq. 7 indicates that the *HET* experiment drives a slight increase in the near-surface  
 342 buoyancy production term due to the enhanced  $\overline{w'\theta_1'}$ , (solid teal line in Fig. 3), but the increase  
 343 is too small to drive a statistically significant response in the total vertical velocity variance.  
 344

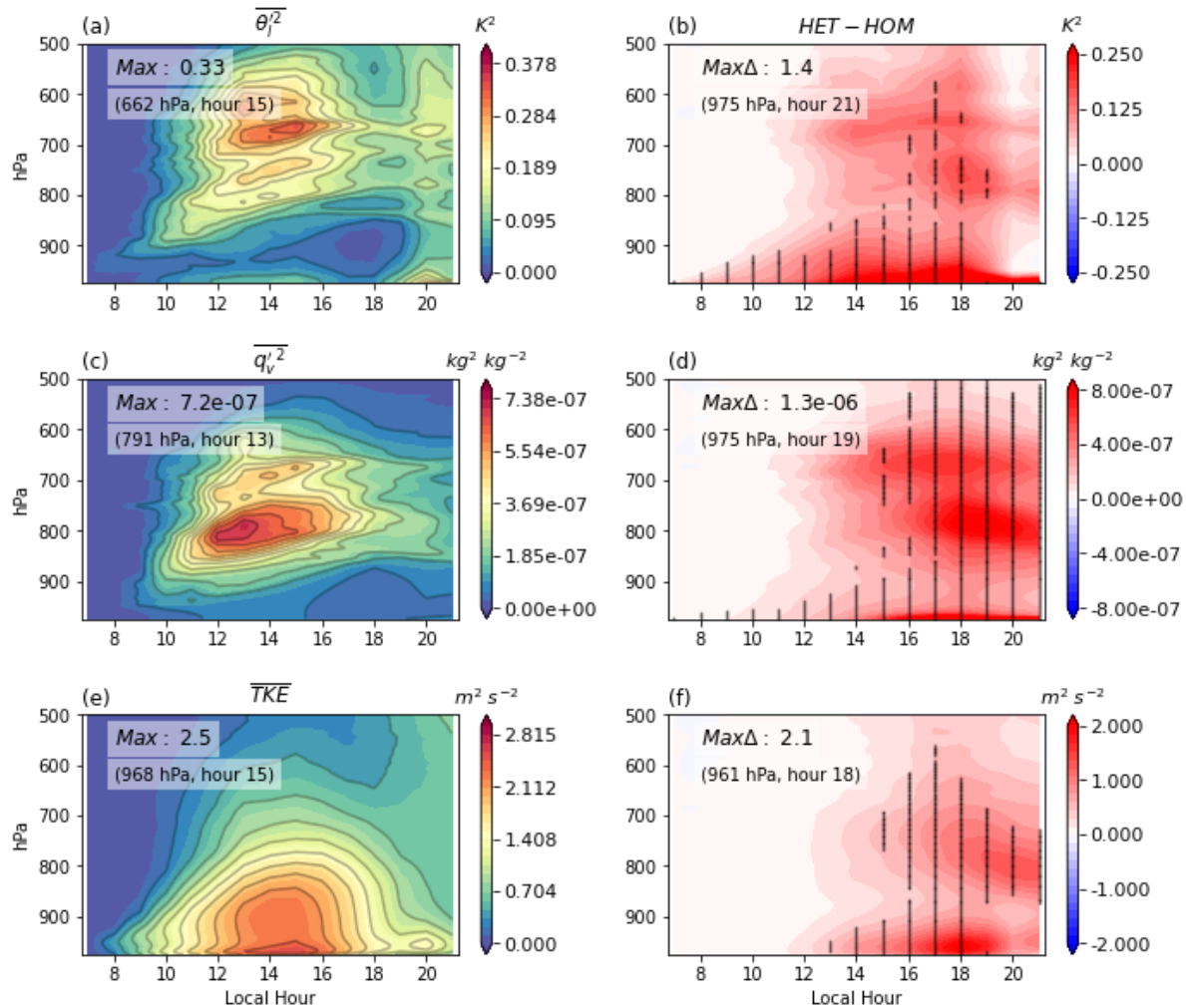


345 **Figure 3:** Mean budget terms of  $\overline{w'^2}$  as in Eq. 7 for (a) *HOM* and (b) *HET-HOM*. Profiles are  
 346 averaged from 17-21 LT, the hours at which the changes in  $\overline{\theta_1'^2}$  are statistically significant.  
 347  
 348

### 349 3.2 Atmospheric response to surface heterogeneity in WRF-LES

350 The above changes in higher-order moments and turbulence in SCAM can be directly compared  
 351 with WRF-LES experiments averaged over the same set of 60 days and driven by higher-  
 352 resolution LASSO-VARANAL forcing (Fig. 4). Again, we emphasize that we do not expect nor  
 353 find agreement between WRF-LES and SCAM *HOM* cases. The two in fact differ substantially,  
 354 with  $\overline{\theta_1'^2}$  reaching a maximum aloft in LES (1.4 K<sup>2</sup> at 662 hPa) rather than near the surface as in  
 355 CLUBB (Fig. 4a). The values of  $\overline{q_t'^2}$  are slightly more similar between models in where they  
 356 peak (~790 hPa in LES vs. 820 hPa in SCAM), though the maximum is more than four times  
 357 larger in LES (Fig. 4c). The lowest level variances themselves can differ markedly between  
 358 models, though again this is not unexpected; potential sources for that disagreement are explored  
 359 further in Section 3.3. Atmospheric turbulence in WRF-LES *HOM* is more than twice as large as  
 360 in SCAM as well, but the peak again occurs near the surface and during the mid-afternoon (Fig.

361 4e). Note that in WRF-LES, TKE is computed as half the sum of the meridional, zonal, and  
 362 vertical velocity variances for consistency with Simon et al. (2021). In both this and SCAM,  
 363 however, the calculation reflects how the different atmospheric models generate turbulence.  
 364



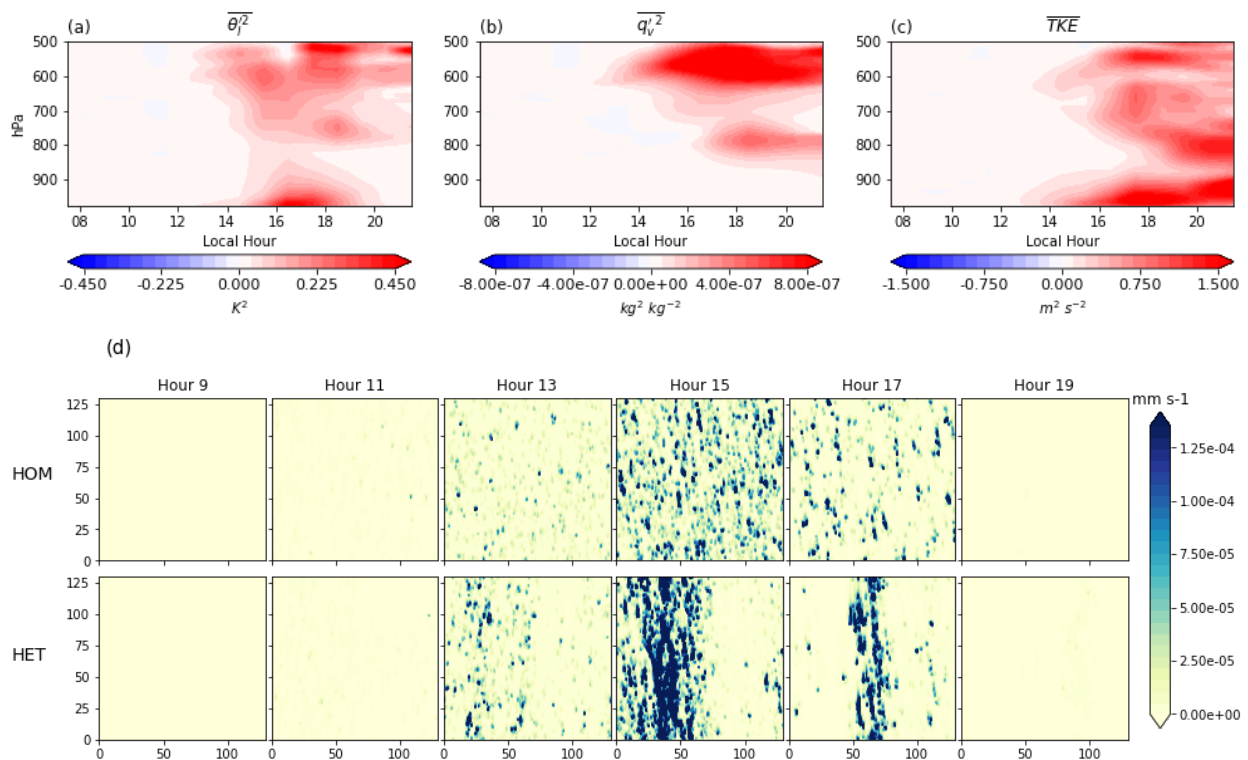
365  
 366 **Figure 4:** As in Figure 1, but for the WRF-LES experiments  
 367

368 In WRF-LES *HET* cases, we find the expected increase in near-surface  $\overline{\theta_i'^2}$  and  $\overline{q_t'^2}$  due to  
 369 spatially varying fluxes (Fig. 4b,d). The largest changes in magnitude are again located near the  
 370 surface and occur in the late evening, suggesting that the SCAM *HET* case is capturing at least  
 371 part of the heterogeneity signal reasonably well. Unlike SCAM, however, significant increases in  
 372 WRF-LES variances extend well beyond the lowest model levels (up to ~575 hPa at 17 LT for  
 373  $\overline{\theta_i'^2}$ , and beyond that for  $\overline{q_t'^2}$ ). But this vertical extension appears to be somewhat disconnected  
 374 from the surface signal, as the magnitude of  $\overline{\theta_i'^2}$  and  $\overline{q_t'^2}$  changes are not continuous. Thus the  
 375 increases that occur at the surface and aloft may result from different physical mechanisms. The  
 376 increased magnitude and extent of these higher-order moments coincides with TKE increases of  
 377 up to 2.1 m<sup>2</sup>/s<sup>2</sup> during the evening, but again there appear to be two centroids to the *HET*  
 378 response, one near the surface and one near 800 hPa (Fig. 4f).

379

380 Assessing individual days in the record rather than the 60-day mean confirms that the elevated  
 381 *HET* increases in WRF-LES are typically separate from the near-surface signal. We hypothesize  
 382 that this is due to the explicit representation of mesoscale secondary circulations that arise  
 383 between warm/dry and cool/wet patches. Those circulations then organize convection and  
 384 rainfall, as illustrated below for the main day assessed by Simon et al. (2021) (Fig. 5). The  
 385 elevated increases in  $\overline{\theta'_t{}^2}$ ,  $\overline{q'_t{}^2}$ , and TKE align with the formation and organization of shallow  
 386 convection around 13-14 LT, and are not directly tied to the surface variance of temperature or  
 387 moisture. This is in agreement with the findings of Simon et al. (2022), who confirm that the  
 388 largest changes in TKE and liquid water path occur as a result of mesoscale secondary  
 389 circulations ( $\mathcal{O}(10\text{ km})$  or greater) in an assessment of all 92 WRF-LES cases. CLUBB, which is  
 390 described by simple continuous PDFs of temperature, moisture, and vertical velocity, is not  
 391 designed to capture the turbulence characteristics of overturning circulations that span the  
 392 gridcell. It is therefore likely that SCAM experiments will be unable to match the vertical  
 393 structure of the WRF-LES *HET* response without additional development efforts to properly  
 394 capture these structures.  
 395

396



397

398 **Figure 5:** A single-day case study (9/24/2017) of WRF-LES HET-HOM (a) moisture variance,  
 399 (b) temperature variance, and (c) TKE; (d) hourly mean snapshots of rainfall in HOM (top) and  
 400 HET (bottom).

401

402 There are, however, additional reasons why the atmospheric response to SGS heterogeneity  
 403 might be expected to differ between SCAM and WRF-LES. From a land surface perspective, the  
 404 subgrid heterogeneity is computed by two different land models in these experiments. CLM5  
 405 provides the surface information to SCAM, but high resolution HydroBlocks simulations are

406 used to provide surface boundary conditions to WRF-LES. The latter ingests observed  
 407 precipitation at a 4 km resolution so that the impact of SGS meteorology is reasonably captured  
 408 across the entire 130x130 km<sup>2</sup> domain. This is especially critical in the central United States,  
 409 where scattered thunderstorms and mesoscale systems are a common feature of the summer  
 410 climatology, but cover less than a full GCM gridcell (i.e.,  $\geq 1^\circ$ ). Their impact on surface  
 411 temperature and moisture variance is thus explicitly included in HydroBlocks but not in CLM5,  
 412 which contributes to differences in the *HOM* cases as well.

413  
 414 From an atmospheric perspective there are potentially critical model differences as well, aside  
 415 from the fact that CLUBB does not represent large-scale secondary circulations. WRF-LES  
 416 includes an explicit representation of convective processes that enables shallow convection to  
 417 transition smoothly into resolved deep convection. While SCAM contains its own deep  
 418 convection parameterization (G. Zhang and MCFarlane, 1995; Neale et al., 2008), it is separated  
 419 from the moist turbulence processes in CLUBB. There is therefore a conceptual jump between  
 420 CLUBB-based shallow convection and deep convection, where the presence of SGS  
 421 heterogeneity is being implicitly conveyed to the deeper atmosphere. A more continuous  
 422 representation of the transition between shallow and deep convection could be important for  
 423 realizing the impacts of surface heterogeneity on the overlying atmosphere. This is particularly  
 424 of interest given the elevated *HET* signal that occurs in WRF-LES but is absent in SCAM.  
 425

### 426 3.3 SCAM Sensitivity Experiments

427 Though some model limitations outlined above require additional parameterization development  
 428 and/or significant model calibration, appropriate testing through sensitivity experiments could  
 429 reveal shortcomings in the existing CLUBB configuration. Two additional sets of SCAM  
 430 experiments are thus conducted to explore the potential impacts of SGS meteorology and of a  
 431 more continuous convection scheme, discussed in turn below.

432  
 433 Scattered sub-grid precipitation is expected to increase SGS temperature and moisture variances  
 434 within CLM5, as only a fraction of the domain would experience soil moisture increases and  
 435 surface cooling. We approximate that impact by scaling the heterogeneous terms in Eq. 4-6 so  
 436 that the grid-mean fluxes and states that define the *HOM* moments remain the same, but the  
 437 difference between surface tiles that produce those values is amplified. The control case (*HOM*)  
 438 is therefore unchanged, but we conduct a new set of heterogeneous surface experiments, *HET*<sub>α</sub>:  
 439

$$440 \quad \overline{\theta_l'^2}_{HET_\alpha} = \overline{\theta_l'^2}_{HOM} + \alpha_\theta * \overline{(\theta_{l,tile} - \bar{\theta}_l)^2} \quad (8)$$

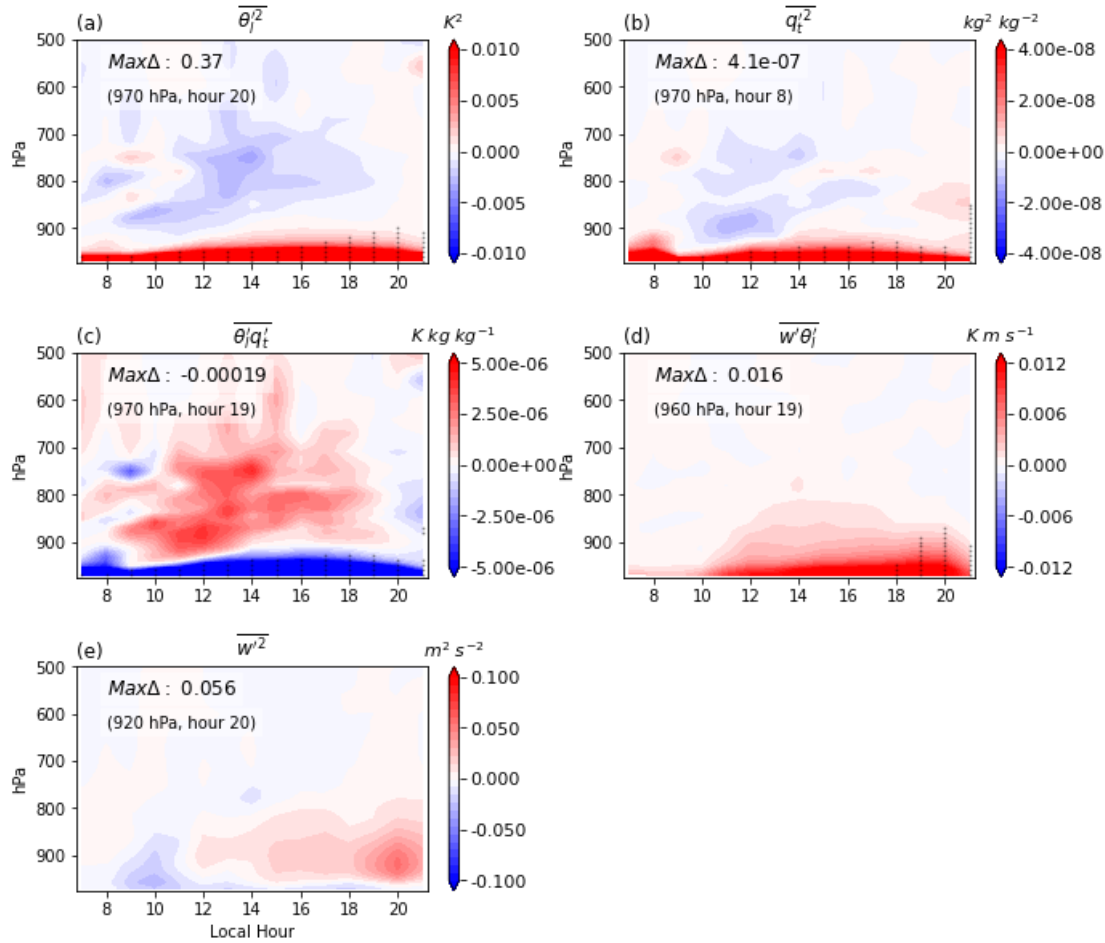
$$441 \quad \overline{q_t'^2}_{HET_\alpha} = \overline{q_t'^2}_{HOM} + \alpha_q * \overline{(q_{t,tile} - \bar{q}_t)^2} \quad (9)$$

$$442 \quad \overline{\theta_l' q_t'}_{HET_\alpha} = \overline{\theta_l' q_t'}_{HOM} + \sqrt{\alpha_\theta} * \sqrt{\alpha_q} * \overline{(\theta_{l,tile} - \bar{\theta}_l)(q_{t,tile} - \bar{q}_t)} \quad (10)$$

443  
 444 The magnitude of the multipliers  $\alpha_\theta$  and  $\alpha_q$  is allowed to vary according to day and is  
 445 determined by comparing the original *HET* cases with the equivalent WRF-LES experiments.  
 446 For each day, the maximum  $\overline{\theta_l'^2}$  and  $\overline{q_t'^2}$  at the lowest model level in WRF-LES is compared to  
 447  
 448

449 the maximum spatial variance at the lowest model level in the SCAM *HET* case. The values of  
 450  $\alpha_\theta$  and  $\alpha_q$  are the ratios of these maxima, designed to ensure nearly equal low-level forcing in  
 451 both model frameworks. On average, this requires values of 51.1 for  $\alpha_\theta$  and 23.9 for  $\alpha_q$ . We also  
 452 conduct a high-end and low-end experiment, where both  $\alpha_\theta$  and  $\alpha_q$  are set to 100 (*HET*<sub>100</sub>) or 10  
 453 (*HET*<sub>10</sub>) for all 60 days. Yet even the *HET* <sub>$\alpha$</sub>  experiment should be considered an upper bound on  
 454 the magnitude of heterogeneity one could expect to represent in SCAM. The lowest level in  
 455 WRF-LES is closer to the surface than in SCAM (~15 m vs. 30 m) and has a much shorter  
 456 timestep (0.5 seconds vs. a 5 minute CLUBB timestep); thus even the *HOM* column-maximum  
 457 variances estimated by CLUBB can be an order of magnitude lower than in WRF-LES.  
 458 Nonetheless, the approach provides an initial indication of how sensitive CAM6 may be to  
 459 surface heterogeneity if LES-type SGS meteorology were represented.

460  
 461 Comparing the atmospheric response in *HET* <sub>$\alpha$</sub>  to *HET*, we find that the vertical extent of  
 462 statistically significant differences in higher order moments increases and spans most of the day  
 463 (*Fig. 6* vs. the right column of *Fig. 1*). At 20 LT, heterogeneity-induced increases in  $\overline{\theta_l'^2}$  peak at  
 464 0.37 K<sup>2</sup> at the lowest model level, but statistically significant increases extend to 900 hPa (*Fig.*  
 465 *6a*). The largest change in  $\overline{q_t'^2}$  occurs at 8 LT, but the largest statistically significant change  
 466 occurs at 16 LT, with small but significant changes extending to 850 hPa at 21 LT (*Fig. 6b*). But  
 467 regardless of how large the surface heterogeneity forcing is, increases in (co)variances are  
 468 confined to pressure levels below 800 hPa and are topped by changes of the opposite sign. Such  
 469 a dipole pattern in the heterogeneity signal is not observed in WRF-LES, where the organization  
 470 of convection and rainfall (again, a phenomenon CLUBB does not capture) likely increases  $\overline{\theta_l'^2}$   
 471 and  $\overline{q_t'^2}$  instead.



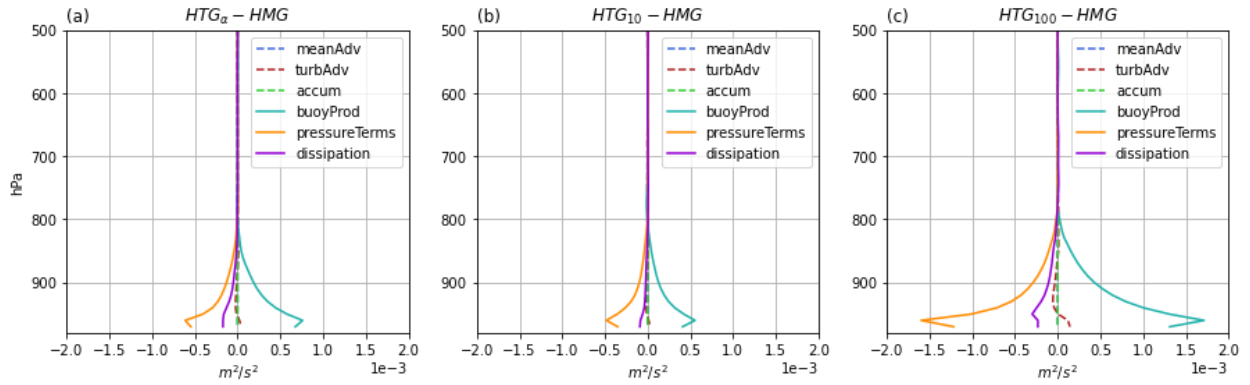
472

473 **Figure 6:** As in the right column of Figure 1, but with differences taken between  $HET_\alpha$  and HOM  
 474 cases.

475

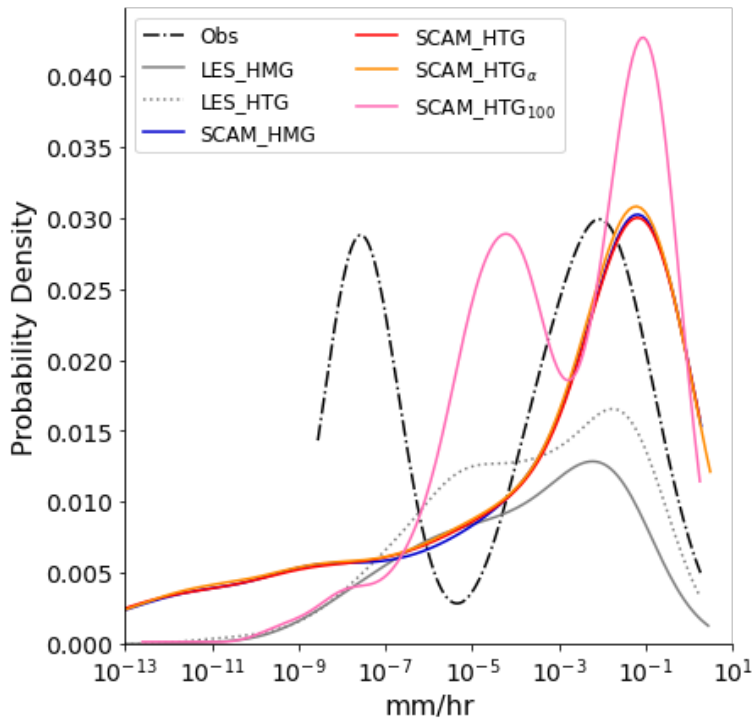
476 Turbulence increases in  $HET_\alpha$  are stronger than those in the original  $HET$  case, but are not  
 477 statistically significant (Fig. 6e), despite significant increases in  $\overline{w'\theta_l'}$  (Fig. 6d). These changes  
 478 are, however, qualitatively similar to the WRF-LES response. As before, we assess the  $\overline{w'^2}$   
 479 budget to assess the mechanism behind the afternoon/evening increase (Fig. 7). The  $HET_{10}$  and  
 480  $HET_{100}$  cases are included for additional context. Compared to Figure 3b, the  $HET$ -scaling  
 481 experiments all induce a stronger and deeper atmospheric response (Fig. 7). The increase in near-  
 482 surface  $\overline{\theta_l'^2}$  drives an increase in the buoyancy production term and a compensating decrease in  
 483 the pressure and dissipation terms. The magnitude and vertical extent of that change scales with  
 484 the magnitude of the surface heterogeneity, with  $HET_{100}$  able to communicate these changes to a  
 485 depth of  $\sim 800$  hPa compared to 850-825 hPa in  $HET_\alpha$  and  $HET_{10}$ .  $HET_{100}$  is also the only case  
 486 to produce statistically significant increases in evening turbulence (not shown). It is therefore  
 487 possible to increase turbulence in SCAM without an explicit representation of mesoscale  
 488 secondary circulations, but it requires a significant increase in the magnitude of surface  
 489 heterogeneity relative to what CLM5 originally predicted.

490



491  
 492 **Figure 7:** As in Figure 3b, but for the three HET-scaling experiments introduced above.  
 493 Averages are again taken from 17-21 LT.  
 494

495 The  $HET_{100}$  case is also the only SCAM experiment to produce a noticeable precipitation change  
 496 (Fig. 8), and is the only one that comes close to producing a similar distribution of hourly mean  
 497 rainfall compared with WRF-LES. The SCAM  $HOM$ ,  $HET$ , and  $HET_\alpha$  cases are all nearly  
 498 identical in their distributions, with a longer tail of near-zero rain rates. These SCAM cases also  
 499 have a single peak in rain rates ( $\sim 0.1$  mm/hr), though both the WRF-LES  $HET$  case and the  
 500 observed rain rates from the LASSO VARANAL dataset (gray and black lines in Fig. 8) are  
 501 bimodal.  $HET_{100}$  produces an appreciable second peak in precipitation and significantly reduces  
 502 the frequency of near-zero rain rates (pink line in Fig. 8). Though the overall shape of the  
 503 distributions are similar between the WRF-LES  $HET$  and SCAM  $HET_{100}$  cases, the discrepancy  
 504 in height between the two suggests that SCAM continues to rain more frequently than WRF-  
 505 LES.  
 506



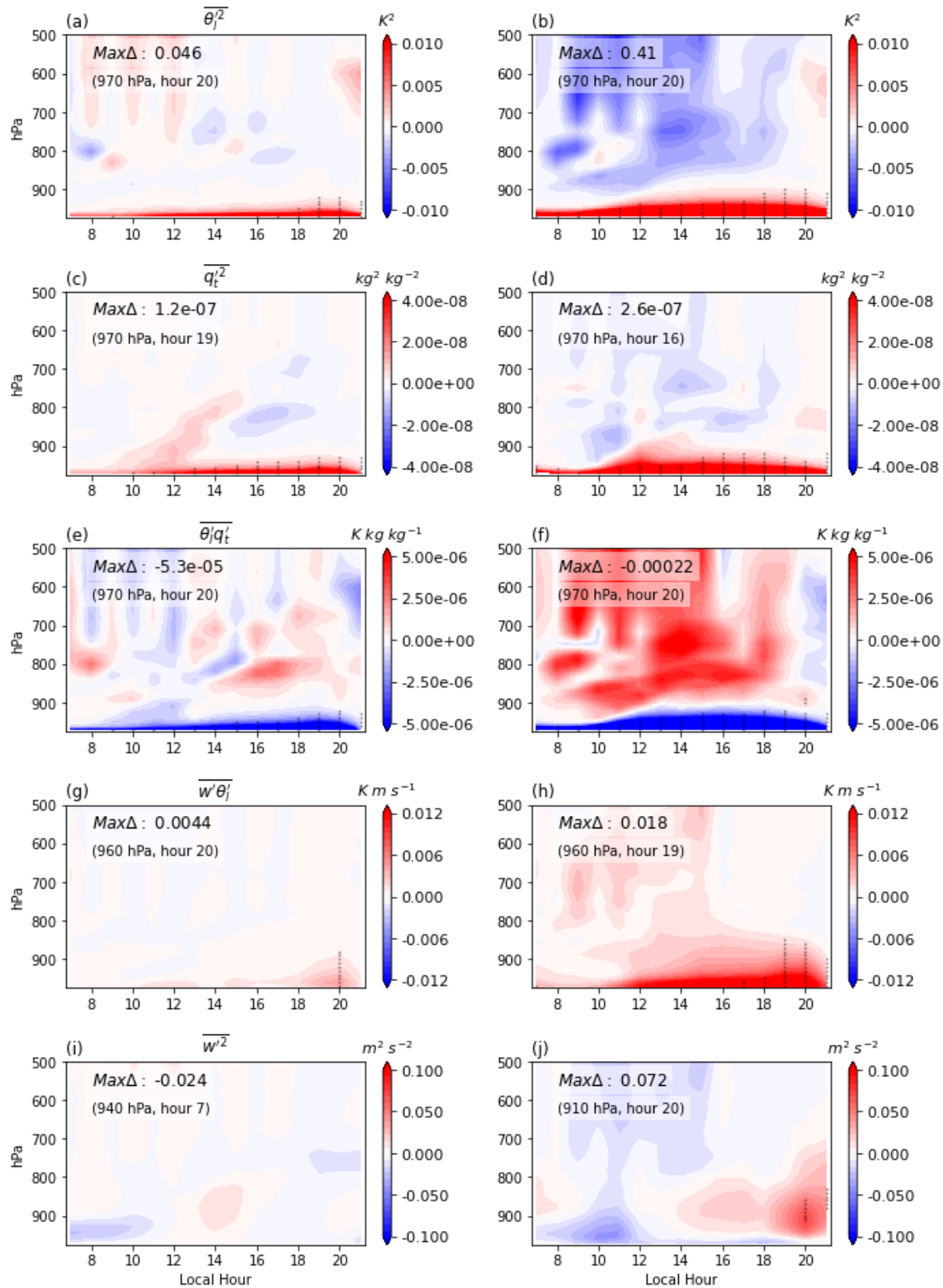
508 **Fig 8:** PDF of hourly mean rain rates in the LASSO VARANAL data set (black dash-dot line),  
 509 WRF-LES (gray lines), and SCAM (colored lines), compiled over all 60 days from 7-23 LT.  
 510 Hours used in constructing the PDF are conditioned on grid-mean rain rates being  $>0$ , such that  
 511 the number of samples varies across simulations if one contains more frequent rainfall.

512  
 513 Although  $HET_{100}$  produces a more sizable turbulence and precipitation response, the magnitude  
 514 of the multiplier is likely unrealistic. Very few days in WRF-LES suggest  $\alpha_\theta$  or  $\alpha_q$  values that  
 515 large, even given the disparity in vertical and temporal resolution between the two models. Seven  
 516 days required  $\alpha_\theta \geq 100$ , and four days required  $\alpha_q \geq 100$ . Thus, while  $HET_{100}$  is useful for  
 517 assessing if any modification of CLUBB's surface boundary conditions can drive a strong  
 518 atmospheric response, this is not a reasonable option for achieving agreement between WRF-  
 519 LES and SCAM.

520  
 521 These scaling experiments suggest that the disagreement in WRF-LES and SCAM responses to  
 522 SGS surface heterogeneity is not solely the result of different surface (co)variance magnitudes.  
 523 We thus explore a second possibility, that the increase in higher-order moments used as  
 524 boundary conditions for CLUBB is not being felt by the deep convection scheme in SCAM,  
 525 thereby limiting the atmospheric response. In this sensitivity test, we define a new set of  
 526 homogeneous and heterogeneous SCAM cases wherein the deep convection scheme is switched  
 527 off; this ensures that CLUBB handles all convection regardless of its characterization as shallow  
 528 or deep (these cases are denoted as  $HOM_{noDC}$  and  $HET_{noDC}$ , respectively). We also test the  
 529 hypothesis that both factors (continuous convection as well as larger surface variances) could  
 530 interact, computing a multiplier for the heterogeneous terms as in  $HET_\alpha$ , but based on the ratio of  
 531  $HET_{noDC}$  and WRF-LES daily maxima; this case will be referred to as  $HET_{\alpha_{noDC}}$ .

532  
 533 Eliminating the separation between shallow and deep convection schemes in SCAM is not  
 534 sufficient to produce a  $\overline{\theta'_t{}^2}$  and  $\overline{q'_t{}^2}$  increase that is consistent with WRF-LES (Fig. 9a,c). In  
 535 general, the signal in  $HET_{noDC}$  is similar to  $HET$  – increases in variances are limited vertically,  
 536 and temporally for  $\overline{\theta'_t{}^2}$ . Turbulence increases slightly, but the change is still not statistically  
 537 significant (Fig. 9i).

538



539  
540  
541  
542

**Figure 9:** As in Figure 6, but for cases without a separate deep convection scheme. (Left)  $HET_{noDC} - HOM_{noDC}$ ; (right)  $HET_{\alpha noDC} - HOM_{noDC}$

543 Increasing the magnitude of surface heterogeneity in  $HET_{\alpha_{noDC}}$  increases the vertical extent of  
544 significant increases in  $\overline{\theta'_l{}^2}$  and  $\overline{q'_t{}^2}$  to 900 hPa and 920 hPa, respectively, and extends the  
545 number of hours at which changes are significant (Fig. 9b,d). Those increases are again  
546 accompanied by a broader low troposphere signal of the opposite sign, but without representing  
547 secondary circulations and the resulting organization of convection, elevated increases are a  
548 difficult WRF-LES feature for SCAM to emulate. Yet  $HET_{\alpha_{noDC}}$  achieves an increase in  
549 evening turbulence that is statistically significant and stretches to 830 hPa (Fig. 9j).

550  
551 Combined, these sensitivity experiments have explored two potential hypotheses for why WRF-  
552 LES and SCAM differ in their response to SGS surface heterogeneity, but neither sufficiently  
553 explains the current disparity. A representation of SGS meteorology combined with a more  
554 continuous convection representation in SCAM both hold promise for improving model  
555 agreement, but additional factors likely play a critical role. It is beyond the scope of the current  
556 study to investigate all of these potential drivers, but a more explicit representation of mesoscale  
557 secondary circulations is likely a necessity in future development efforts based on the results of  
558 Simon et al. (2022) and the current SCAM shortcomings shown here.  
559

#### 560 **4 Discussion and Conclusions**

561 In this study, we explored a new CESM2 coupling strategy designed to capture the impacts of  
562 SGS surface heterogeneity on the atmosphere. The approach links information on the distribution  
563 of temperature and moisture across surface tiles in CLM5 with CLUBB's boundary conditions in  
564 CAM6. To investigate the impact of this new addition, a series of SCAM experiments were  
565 conducted at the ARM SGP site on 60 warm season shallow convection days, which were  
566 compared to a similar existing set of WRF-LES simulations (Simon et al., 2021, 2022). Although  
567 LES output should not be conflated with observations (there is no guarantee that the WRF-LES  
568 sensitivity to heterogeneity is accurate), the experiments offer a unique opportunity to explicitly  
569 isolate the role of surface heterogeneity each day and its impact on higher order, difficult to  
570 observe variables.

571  
572 In WRF-LES, SGS heterogeneity increases the grid-mean variance of temperature and moisture,  
573 with statistically significant differences relative to *HOM* that grow in the vertical during the  
574 afternoon to depths of nearly 500 hPa. There are two unique centroids within this atmospheric  
575 response - one near the surface, and another more elevated one that becomes apparent in the late  
576 afternoon. The latter is hypothesized to result from mesoscale secondary circulations initiated by  
577 variability in surface sensible and latent heat fluxes in the *HET* case. These structures increase  
578 afternoon/evening TKE and help organize convection and precipitation (Simon et al., 2022).  
579

580 The SCAM parameterization produces a markedly weaker atmospheric response to  
581 heterogeneity. Increases in *HET* temperature and moisture variances are smaller than those in  
582 WRF-LES, and are more constrained vertically and temporally. This results in no discernable  
583 increase in turbulence. We attempt to diagnose the reason for such a limited atmospheric  
584 response through a series of additional experiments that isolate important model differences  
585 between WRF-LES and SCAM.  
586

587 The WRF-LES experiments are forced at the surface by a high-resolution land model that  
588 captures the impacts of SGS meteorology on soil moisture and temperature. CLM5 does not yet  
589 have a similar capability, though recent developments do enable the downscaling of incoming  
590 radiation, temperature, and precipitation due to variations in topography (Swenson et al., 2019).  
591 The SGP site is fairly uniform in elevation however, such that this downscaling has little to no  
592 impact on the computed variances of temperature and humidity. Instead, we approximate the  
593 effect of scattered storms by applying a scaling factor that artificially increases the magnitude of  
594 heterogeneity within the gridcell ( $HET_\alpha$ ,  $HET_{10}$ , and  $HET_{100}$ ). Though this approach does  
595 slightly increase the vertical and temporal extent of significant differences in the (co)variances of  
596 temperature and moisture, it is still unable to generate a statistically significant heterogeneous  
597 signal similar to that in WRF-LES. Only in the  $HET_{100}$  case are differences in  $\overline{w'^2}$  statistically  
598 significant, as the surface boundary conditions used in CLUBB are large enough to drive a large  
599 and deep increase in buoyancy production through enhanced turbulent fluxes of virtual potential  
600 temperature. This is also the only experiment capable of producing altered precipitation statistics  
601 that align with some aspects of WRF-LES (e.g., bimodal distributions with limited near-zero rain  
602 rates). Despite these encouraging signs, the magnitude of the scaling applied is likely unrealistic.  
603

604 Another important difference between the SCAM and LES models is in their representation of  
605 convection. The high vertical, horizontal, and temporal resolutions used in LES explicitly  
606 resolves the continuous transition between shallow and deep convection without an artificial  
607 switch between convective parameterizations; the same cannot be said for SCAM. We thus  
608 experiment with turning off the deep convection scheme and allowing CLUBB to handle all  
609 convection that develops in the grid, even if it grows to deeper levels. While the  $HET_{noDC}$   
610 experiment indicates a small but not significant increase in turbulence,  $\overline{\theta_l'^2}$ ,  $\overline{q_t'^2}$ , and  $\overline{\theta_l'q_t'}$   
611 continue to respond only near the surface. Combining our two sensitivity experiments by  
612 applying a multiplier to the cases without a separate deep convection scheme,  $HET_{\alpha,noDC}$  comes  
613 close to qualitatively agreeing with WRF-LES, though heterogeneity-induced changes continue  
614 to be vertically limited.  
615

616 The above sensitivity experiments are not sufficient to definitively answer the question of what  
617 causes the difference in WRF-LES and SCAM responses to SGS heterogeneity, but they do  
618 highlight the complex nature of the problem. Critically, the current SCAM parameterization  
619 lacks the ability to explicitly represent secondary circulations, which Simon et al. (2022) suggest  
620 are critical to the atmospheric response present in these WRF-LES experiments. In other  
621 observational and LES experiments as well, the atmospheric differences that arise over  
622 heterogeneous surfaces stem from these mesoscale secondary circulations that transport heat and  
623 moisture between parts of the domain (Cioni & Hohenegger, 2018; Avissar & Schmidt, 1998;  
624 Doran et al., 1995; Ookouchi et al., 1984). Such circulations are currently outside the scope of  
625 what CLUBB is designed to capture in its statistical representation of SGS heterogeneity, and the  
626 parameterization implemented here was not intended to add that phenomenon to the model.  
627 Instead, the intent was to capture the impact these circulations have on surface variances and  
628 back out a response in CLUBB through that pathway alone. It is likely, however, that further  
629 development efforts will require a more thorough representation of secondary circulations to  
630 create a more realistic atmospheric response to surface heterogeneity. Ongoing work to represent  
631 not only eddy diffusivity (as in CLUBB) but also mass fluxes within climate models thus holds  
632 particular promise for its ability to mix surface states and fluxes more thoroughly in the vertical.

633 Future work should focus on pathways to communicate the impacts of surface heterogeneity to  
634 the atmosphere not just through surface boundary conditions but in ways that can influence the  
635 vertical and horizontal transport of energy and moisture in a spatially organized manner.

636

### 637 **Acknowledgments**

638 Funding for this work was provided by NOAA grants NA19OAR4310241 and  
639 NA19OAR4310242. Additional support for MDF was provided through NSF award 1755088.

640

### 641 **Open Research**

642 Simulations are run with a modified version of CESM2 that enables the calculation of CLUBB's  
643 surface boundary conditions in the land model; the model source code including these  
644 modifications, SCAM model output, and analysis scripts are available at Fowler et al. (2022).

645 The WRF-LES model output is currently publicly available from

646 <http://hydrology.cee.duke.edu/CLASP/LES/diags2/>.

647

### 648 **References**

649 André, J. C., de Moor, G., Lacarrere, P., Therry, G., & du Vachat, R. (1978). Modeling the 24-  
650 hour evolution of the mean and turbulent structures of the planetary boundary layer. *Journal of*  
651 *the Atmospheric Sciences*, 35, 1861–1883. [https://doi.org/10.1175/1520-](https://doi.org/10.1175/1520-0469(1978)035<1861:MTHEOT>2.0.CO;2)  
652 [0469\(1978\)035<1861:MTHEOT>2.0.CO;2](https://doi.org/10.1175/1520-0469(1978)035<1861:MTHEOT>2.0.CO;2)

653 Avissar, R., & Liu, Y. (1996). Three-dimensional numerical study of shallow convective clouds  
654 and precipitation induced by land surface forcing. *Journal of Geophysical Research:*  
655 *Atmospheres*, 101(D3), 7499–7518. <https://doi.org/10.1029/95JD03031>

656 Avissar, R., & Pielke, R. (1989). A parameterization of heterogeneous land surfaces for  
657 atmospheric numerical models and its impact on regional meteorology. *Monthly Weather*  
658 *Review*, 117, 2113–2136. [https://doi.org/10.1175/1520-](https://doi.org/10.1175/1520-0493(1989)117<2113:APOHLS>2.0.CO;2)  
659 [0493\(1989\)117<2113:APOHLS>2.0.CO;2](https://doi.org/10.1175/1520-0493(1989)117<2113:APOHLS>2.0.CO;2)

660 Avissar, R., & Schmidt, T. (1998). An evaluation of the scale at which ground-surface heat flux  
661 patchiness affects the convective boundary layer using large-eddy simulations. *Journal of the*  
662 *Atmospheric Sciences*, 55, 2666–2689. [https://doi.org/10.1175/1520-](https://doi.org/10.1175/1520-0469(1998)055<2666:AEOTSA>2.0.CO;2)  
663 [0469\(1998\)055<2666:AEOTSA>2.0.CO;2](https://doi.org/10.1175/1520-0469(1998)055<2666:AEOTSA>2.0.CO;2)

- 664 Baik, J. J., Kim, Y. H., & Chun, H. Y. (2001). Dry and moist convection forced by an urban heat  
665 island. *Journal of Applied Meteorology*, *40*(8), 1462–1475. [https://doi.org/10.1175/1520-0450\(2001\)040<1462:DAMCFB>2.0.CO;2](https://doi.org/10.1175/1520-0450(2001)040<1462:DAMCFB>2.0.CO;2)
- 667 Berg, L. K., & Stull, R. B. (2005). A simple parameterization coupling the convective daytime  
668 boundary layer and fair-weather cumuli. *Journal of the Atmospheric Sciences*, *62*(6), 1976–1988.  
669 <https://doi.org/10.1175/JAS3437.1>
- 670 Bou-Zeid, E., Anderson, W., Katul, G. G., & Mahrt, L. (2020). The persistent challenge of  
671 surface heterogeneity in boundary-layer meteorology: A review. *Boundary-Layer Meteorology*,  
672 *177*, 227–245. <https://doi.org/10.1007/s10546-020-00551-8>
- 673 Brunsell, N. A., Mechem, D. B., & Anderson, M. C. (2011). Surface heterogeneity impacts on  
674 boundary layer dynamics via energy balance partitioning. *Atmospheric Chemistry and Physics*,  
675 *11*, 3403–3416. <https://doi.org/10.5194/acp-11-3403-2011>
- 676 Chaney, N. W., Metcalfe, P., & Wood, E. F. (2016). HydroBlocks: a field-scale resolving land  
677 surface model for application over continental extents. *Hydrological Processes*, *30*(20), 3543–  
678 3559. <https://doi.org/https://doi.org/10.1002/hyp.10891>
- 679 Cheng, Y., Chan, P. W., Wei, X., Hu, Z., Kuang, Z., & McColl, K. A. (2021). Soil moisture  
680 control of precipitation reevaporation over a heterogeneous land surface. *Journal of the*  
681 *Atmospheric Sciences*, *78*(10), 3369–3383. <https://doi.org/10.1175/JAS-D-21-0059.1>
- 682 Cioni, G., & Hohenegger, C. (2018). A simplified model of precipitation enhancement over a  
683 heterogeneous surface. *Hydrology and Earth System Sciences*, *22*(6), 3197–3212.  
684 <https://doi.org/10.5194/hess-22-3197-2018>
- 685 Dai, Y., Zeng, X., Dickinson, R. E., Baker, I., Bonan, G. B., Bosilovich, M. G., et al. (2003). The  
686 common land model experience. *Bulletin of the American Meteorological Society*, *84*(8), 1013–  
687 1024. <https://doi.org/https://doi.org/10.1175/BAMS-84-8-1013>
- 688 Dirmeyer, P. A., Balsamo, G., Blyth, E. M., Morrison, R., & Cooper, H. M. (2021). Land-  
689 Atmosphere Interactions Exacerbated the Drought and Heatwave Over Northern Europe During  
690 Summer 2018. *AGU Advances*, *2*(2), 1–16. <https://doi.org/10.1029/2020av000283>
- 691 Dixon, P. G., & Mote, T. L. (2003). Patterns and causes of Atlanta’s urban heat island-initiated  
692 precipitation. *Journal of Applied Meteorology*, *42*(9), 1273–1284. [https://doi.org/10.1175/1520-0450\(2003\)042<1273:PACOAU>2.0.CO;2](https://doi.org/10.1175/1520-0450(2003)042<1273:PACOAU>2.0.CO;2)
- 694 Doran, J. C., Shaw, W. J., & Hubbe, J. M. (1995). Boundary layer characteristics over areas of  
695 inhomogeneous surface fluxes. *Journal of Applied Meteorology*, *34*, 559–571.  
696 <https://doi.org/https://doi.org/10.1175/1520-0450-34.2.559>
- 697 Fischer, E. M., Seneviratne, S. I., Lüthi, D., & Schär, C. (2007). Contribution of land-atmosphere  
698 coupling to recent European summer heat waves. *Geophysical Research Letters*, *34*(6), 1–6.  
699 <https://doi.org/10.1029/2006GL029068>
- 700 Fowler, M. D., Neale, R. B., Simon, J. S., Lawrence, D. M., Chaney, N. W., Dirmeyer, P. A., et  
701 al. (2022, November). Assessing the atmospheric response to subgrid surface heterogeneity in  
702 CESM2 - code, output, and analysis script [Dataset]. *Zenodo*.  
703 <https://doi.org/10.5281/zenodo.7308152>
- 704 Gettelman, A., Truesdale, J. E., Bacmeister, J. T., Caldwell, P. M., Neale, R. B., Bogenschutz, P.

- 705 A., & Simpson, I. R. (2019). The Single Column Atmosphere Model Version 6 (SCAM6): Not a  
706 scam but a tool for model evaluation and development. *Journal of Advances in Modeling Earth*  
707 *Systems*, 11(5), 1381–1401. <https://doi.org/10.1029/2018MS001578>
- 708 Golaz, J. C., Larson, V. E., & Cotton, W. R. (2002). A PDF-based model for boundary layer  
709 clouds. Part I: Method and model description. *Journal of the Atmospheric Sciences*, 59, 3540–  
710 3551. [https://doi.org/10.1175/1520-0469\(2002\)059<3540:APBMFB>2.0.CO;2](https://doi.org/10.1175/1520-0469(2002)059<3540:APBMFB>2.0.CO;2)
- 711 Graf, M., Arnault, J., Fersch, B., & Kunstmann, H. (2021). Is the soil moisture precipitation  
712 feedback enhanced by heterogeneity and dry soils? A comparative study. *Hydrological*  
713 *Processes*, 35(9), 1–15. <https://doi.org/10.1002/hyp.14332>
- 714 Gustafson, W. I., Vogelmann, A. M., Cheng, X., Dumas, K. K., Endo, S., Johnson, K. L., et al.  
715 (2019). *Description of the LASSO data bundles product*. <https://doi.org/10.2172/1469590>
- 716 Hahmann, A. N., & Dickinson, R. E. (2001). A fine-mesh land approach for general circulation  
717 models and its impact on regional climate. *Journal of Climate*, 14(7), 1634–1646.  
718 [https://doi.org/10.1175/1520-0442\(2001\)014<1634:AFMLAF>2.0.CO;2](https://doi.org/10.1175/1520-0442(2001)014<1634:AFMLAF>2.0.CO;2)
- 719 Hirschi, M., Seneviratne, S. I., Alexandrov, V., Boberg, F., Boroneant, C., Christensen, O. B., et al.  
720 (2011). Observational evidence for soil-moisture impact on hot extremes in southeastern  
721 Europe. *Nature Geoscience*, 4, 17–21. <https://doi.org/10.1038/ngeo1032>
- 722 Hjelmfelt, M. R. (1982). Numerical simulation of the effects of St. Louis on mesoscale  
723 boundary-layer airflow and vertical air motion: Simulations of urban vs. non-urban effects.  
724 *Journal of Applied Meteorology*, 21, 1239–1257. [https://doi.org/https://doi.org/10.1175/1520-0450\(1982\)021%3C1239:NSOTEO%3E2.0.CO;2](https://doi.org/https://doi.org/10.1175/1520-0450(1982)021%3C1239:NSOTEO%3E2.0.CO;2)
- 726 Huang, H. Y., & Margulis, S. A. (2013). Impact of soil moisture heterogeneity length scale and  
727 gradients on daytime coupled land-cloudy boundary layer interactions. *Hydrological Processes*,  
728 27, 1988–2003. <https://doi.org/10.1002/hyp.9351>
- 729 Huang, M., Ma, P.-L., Chaney, N. W., Hao, D., Bisht, G., Fowler, M. D., et al. (2022).  
730 Representing surface heterogeneity in land-atmosphere coupling in E3SMv1 single-column  
731 model over ARM SGP during summertime. *Geoscientific Model Development Discussions*,  
732 2022, 1–20. <https://doi.org/10.5194/gmd-2021-421>
- 733 Hubbe, J. M., Doran, J. C., Liljegren, J. C., & Shaw, W. J. (1997). Observations of spatial  
734 variations of boundary layer structure over the southern great plains cloud and radiation testbed.  
735 *Journal of Applied Meteorology*, 36(9), 1221–1231. [https://doi.org/10.1175/1520-0450\(1997\)036<1221:OOSVOB>2.0.CO;2](https://doi.org/10.1175/1520-0450(1997)036<1221:OOSVOB>2.0.CO;2)
- 737 Kang, S. L. (2016). Regional bowen ratio controls on afternoon moist convection: A large eddy  
738 simulation study. *Journal of Geophysical Research: Atmospheres*, 121, 14,056–14,083.  
739 <https://doi.org/10.1002/2016JD025567>
- 740 Koster, R. D., & Suarez, M. J. (1992). Modeling the land surface boundary in climate models as  
741 a composite of independent vegetation stands. *Journal of Geophysical Research*, 97(D3), 2697–  
742 2715. <https://doi.org/10.1029/91JD01696>
- 743 Kustas, W. P., & Albertson, J. D. (2003). Effects of surface temperature contrast on land-  
744 atmosphere exchange: A case study from Monsoon 90. *Water Resources Research*, 39, 1–11.  
745 <https://doi.org/10.1029/2001WR001226>

- 746 Larson, V. E. (2017). CLUBB-SILHS: A parameterization of subgrid variability in the  
747 atmosphere. arXiv. <https://doi.org/10.48550/ARXIV.1711.03675>
- 748 Larson, V. E., Golaz, J. C., & Cotton, W. R. (2002). Small-scale and mesoscale variability in  
749 cloudy boundary layers: Joint probability density functions. *Journal of the Atmospheric Sciences*,  
750 *59*(24), 3519–3539. [https://doi.org/10.1175/1520-0469\(2002\)059<3519:SSAMVI>2.0.CO;2](https://doi.org/10.1175/1520-0469(2002)059<3519:SSAMVI>2.0.CO;2)
- 751 Lawrence, D. M., Fisher, R. A., Koven, C. D., Oleson, K. W., Swenson, S. C., Bonan, G., et al.  
752 (2019). The Community Land Model Version 5: Description of new features, benchmarking, and  
753 impact of forcing uncertainty. *Journal of Advances in Modeling Earth Systems*, *11*(12), 4245–  
754 4287. <https://doi.org/10.1029/2018MS001583>
- 755 Li, D., Bou-Zeid, E., Barlage, M., Chen, F., & Smith, J. A. (2013). Development and evaluation  
756 of a mosaic approach in the WRF-Noah framework. *Journal of Geophysical Research*  
757 *Atmospheres*, *118*(21), 11,918–11,935. <https://doi.org/10.1002/2013JD020657>
- 758 Machulskaya, E., & Mironov, D. (2018). Boundary conditions for scalar (co)variances over  
759 heterogeneous surfaces. *Boundary-Layer Meteorology*, *169*, 139–150.  
760 <https://doi.org/10.1007/s10546-018-0354-6>
- 761 Mahrt, L. (2000). Surface heterogeneity and vertical structure of the boundary layer. *Boundary-*  
762 *Layer Meteorology*, *96*, 33–62. <https://doi.org/10.1023/A:1002482332477>
- 763 Mocko, D. M., Kumar, S. V., Peters-Lidard, C. D., & Wang, S. (2021). Assimilation of  
764 vegetation conditions improves the representation of drought over agricultural areas. *Journal of*  
765 *Hydrometeorology*, *22*(5), 1085–1098. <https://doi.org/10.1175/JHM-D-20-0065.1>
- 766 Neale, R. B., Richter, J. H., & Jochum, M. (2008). The impact of convection on ENSO: From a  
767 delayed oscillator to a series of events. *Journal of Climate*, *21*(22), 5904–5924.  
768 <https://doi.org/10.1175/2008JCLI2244.1>
- 769 Ookouchi, Y., Segal, M., Kessler, R. C., & Pielke, R. A. (1984). Evaluation of soil moisture  
770 effects on the generation and modification of mesoscale circulations. *Monthly Weather Review*,  
771 *112*. [https://doi.org/10.1175/1520-0493\(1984\)112,2281:EOSMEO.2.0.CO;2](https://doi.org/10.1175/1520-0493(1984)112,2281:EOSMEO.2.0.CO;2)
- 772 Pielke Sr., R. A. (2001). Influence of the spatial distribution of vegetation and soils on the  
773 prediction of cumulus convective rainfall. *Reviews of Geophysics*, *39*, 151–177.  
774 <https://doi.org/doi:10.1029/1999RG000072>
- 775 Ramos da Silva, R., Gandu, A. W., Sá, L. D. A., & Dias, M. A. F. S. (2011). Cloud streets and  
776 land-water interactions in the Amazon. *Biogeochemistry*, *105*(1), 201–211.  
777 <https://doi.org/10.1007/s10533-011-9580-4>
- 778 Rieck, M., Hohenegger, C., & van Heerwaarden, C. C. (2014). The influence of land surface  
779 heterogeneities on cloud size development. *Monthly Weather Review*, *142*(10), 3830–3846.  
780 <https://doi.org/10.1175/MWR-D-13-00354.1>
- 781 Santanello, J. A., Roundy, J., & Dirmeyer, P. A. (2015). Quantifying the land-atmosphere  
782 coupling behavior in modern reanalysis products over the U.S. southern great plains. *Journal of*  
783 *Climate*, *28*(14), 5813–5829. <https://doi.org/10.1175/JCLI-D-14-00680.1>
- 784 Schrieber, K., Stull, R., & Zhang, Q. (1996). Distributions of surface-layer buoyancy versus  
785 lifting condensation level over a heterogeneous land surface. *Journal of the Atmospheric*  
786 *Sciences*, *53*, 1086–1107. <https://doi.org/https://doi.org/10.1175/1520->

- 787 0469(1996)053%3C1086:DOSLBV%3E2.0.CO;2
- 788 Shem, W., & Shepherd, M. (2009). On the impact of urbanization on summertime thunderstorms  
789 in Atlanta: Two numerical model case studies. *Atmospheric Research*, *92*(2), 172–189.  
790 <https://doi.org/10.1016/j.atmosres.2008.09.013>
- 791 Shepherd, J. M. (2005). A review of current investigations of urban-induced rainfall and  
792 recommendations for the future. *Earth Interactions*, *9*(12). <https://doi.org/10.1175/EI156.1>
- 793 Simon, J.S., Bragg, A. D., Chaney, N.W. (2022). Spatial organization of surface fluxes leads to  
794 appreciable impacts in the development of shallow convection. Manuscript in preparation for  
795 submission to *Geophysical Research Letters*.
- 796 Simon, J. S., Bragg, A. D., Dirmeyer, P. A., & Chaney, N. W. (2021). Semi-coupling of a field-  
797 scale resolving Land-surface model and WRF-LES to investigate the influence of land-surface  
798 heterogeneity on cloud development. *Journal of Advances in Modeling Earth Systems*, *13*.  
799 <https://doi.org/10.1029/2021MS002602>
- 800 Skamarock, W. C., Klemp, J. B., Dudhia, J., Gill, D. O., Barker, D. M., Wang, W., & Powers, J.  
801 G. (2005). *A description of the advanced research WRF version 2*. (NCAR/TN-475+STR).  
802 NCAR Technical Note.
- 803 Swenson, S. C., Clark, M., Fan, Y., Lawrence, D. M., & Perket, J. (2019). Representing  
804 intrahillslope lateral subsurface flow in the Community Land Model. *Journal of Advances in*  
805 *Modeling Earth Systems*, *11*(12), 4044–4065. <https://doi.org/10.1029/2019MS001833>
- 806 Taylor, C. M., Gounou, A., Guichard, F., Harris, P. P., Ellis, R. J., Couvreux, F., & De Kauwe,  
807 M. (2011). Frequency of sahelian storm initiation enhanced over mesoscale soil-moisture  
808 patterns. *Nature Geoscience*, *4*(7), 430–433. <https://doi.org/10.1038/ngeo1173>
- 809 Zhang, G. J., & McFarlane, N. A. (1995). Sensitivity of climate simulations to the  
810 parameterization of cumulus convection in the canadian climate centre general circulation model.  
811 *Atmosphere - Ocean*, *33*(3), 407–446. <https://doi.org/10.1080/07055900.1995.9649539>
- 812 Zhang, Y., Huang, Q., Ma, Y., Luo, J., Wang, C., Li, Z., & Chou, Y. (2021). Large eddy  
813 simulation of boundary-layer turbulence over the heterogeneous surface in the source region of  
814 the Yellow River. *Atmospheric Chemistry and Physics*, *21*(20), 15949–15968.  
815 <https://doi.org/10.5194/acp-21-15949-2021>
- 816